

Relating the Turbulent Solar Wind Spectral Break at Ion Scales with an Upstream Spectral Bump at Planetary Bow Shocks

M. TERRES  ¹ AND GANG LI  ²

¹*Department of Space Sciences, University of Alabama in Huntsville, USA, mrt0016@uah.edu*

²*Department of Space Sciences, University of Alabama in Huntsville, USA, gangli.uah@gmail.com*

ABSTRACT

At scales much larger than the ion inertial scale and the gyro-radius of thermal protons, Magnetohydrodynamics (MHD) theory is well equipped to describe the nature of solar wind turbulence. The turbulent spectrum itself is defined by a power law manifesting the energy cascading process. A break in the turbulence spectrum develops at smaller scales, signaling the onset of energy dissipation. The exact mechanism for the spectral break is still a matter of debate. In this work, we use the 20 Hz *MESSENGER* magnetic field data during four planetary flybys at different heliocentric distances to examine the nature of the spectral break in solar wind turbulence. By carefully selecting the spacecraft trajectory, we relate the spectral break in the quiet solar wind with a well-known upstream wave phenomenon at planetary bow shocks which is the characteristic spectral bump at frequencies ~ 1 Hz. We identify both spectral breaks and spectral bumps in the turbulence spectrum during four planetary flybys and examine the radial dependence of the ratio of these two frequencies. We argue that the spectral break likely occurs at the cyclotron resonance scale more than the inertial length scale.

Keywords: plasmas - solar wind - Sun: heliosphere - turbulence - waves

1. INTRODUCTION

Turbulence in the solar wind consists of fluctuations across various scales. Nonlinear interactions cascade energy, through the inertial range, across several frequency (wavenumber) decades with a Kolmogorov $k^{-5/3}$ scaling (Bruno & Carbone 2013). Upon reaching ion kinetic scales, the power spectral density of magnetic field fluctuations develops a break, above which the turbulent cascade steepens into a power-law with an index often in the range of -2 to -4 (Leamon et al. 1998; Smith et al. 2006; Alexandrova et al. 2013). The ion kinetic scale frequency is associated with various dissipation or dispersive mechanisms that lead to heating of the surrounding plasma. The differences between dispersive or dissipation mechanisms have been investigated recently (Bowen et al. 2020).

Three ion kinetic scales that have been suggested to cause the spectral break. The first is the ion inertial length scale, $\lambda_i = c/\omega_{pi} = V_A/\Omega_p$, and the second is the ion Larmor radius, $R_L = v_{th}/\Omega_p$. Here $\omega_{pi} = \sqrt{(4\pi n_i q^2)/m_i}$ and $\Omega_p = qB/m_i c$ are the ion plasma frequency and ion cyclotron frequency respectively with c the speed of light and v_{th} the thermal speed of protons. The ion inertial length is associated with the thickness of current sheets. Current sheets have long been recognized as a significant place for plasma heating through magnetic reconnection (Leamon et al. 2000). Ion inertial length scale is also related to the Hall effect, which also represents another mechanism for efficient

dissipation (Bourouaine et al. 2012). In contrast, the Larmor radius is associated with Landau damping of Alfvén waves that heats the surrounding ion population (Schekochihin et al. 2009). The corresponding wave numbers for R_L and λ_i are represented as $k_L = 1/R_L$ and $k_i = 1/\lambda_i = k_d\beta_p^{1/2}$ respectively, where $\beta_p = (V_{th}/V_A)^2$ is the plasma beta. The third scale is the cyclotron resonance scale, in which parallel propagating Alfvén waves exchange energy with the surrounding thermal ion population through the cyclotron resonance $\omega_r + k_{\parallel}v_{th} = \Omega_p$ (Leamon et al. 1998a; Smith et al. 2006; Bruno & Trenchi 2014; Woodham et al. 2018). Under the assumption that $\omega_r \ll \Omega_p$, the minimum resonant wavenumber is $k_d = \Omega_p/(v_A + v_{th}) = k_L/(1 + \beta^{-1/2})$. At 1 AU the inertial length and the Larmor radius are similar because plasma beta $\beta = (V_{th}/V_A)^2$ is close to unity. Furthermore various physical processes can occur simultaneously in the solar wind. Therefore identifying the underlying mechanism for the spectral break has been difficult (Chen et al. 2014; Verscharen et al. 2019).

By examining how the spectral break location varies with heliocentric distances, Perri et al. (2010) and Bourouaine et al. (2012) suggested that the break location, invariant of distance, agreed with the ion inertial scale. However, a later study by Bruno & Trenchi (2014) who made use of special radial alignments of three spacecraft in the solar wind (*MESSENGER*, *Wind*, and *Ulysses*), showed that the break location agrees best with the ion cyclotron resonance scale as first predicted by Leamon et al. (1998a). Telloni et al. (2015) investigated the high-frequency magnetic fluctuations beyond the spectral break, for the periods identified by Bruno & Trenchi (2014). They find that the characteristics are compatible with both left-hand outward-propagating ion cyclotron waves and right-hand kinetic Alfvén waves (Telloni et al. 2015). The existence of kinetic Alfvén waves and ion cyclotron waves found near the break location implies that the dissipation can be associated with ion-cyclotron resonance and/or Landau damping (Telloni et al. 2015).

At 1 AU, the plasma beta of solar wind is often close to 1, so the two scales k_d^{-1} and k_i^{-1} are close to each other. Noticing this, Chen et al. (2014) identified intervals that have extreme value of β_{\perp} ($\ll 1$ and $\gg 1$ respectively) and studied the location of the spectral break. These authors found that for $\beta_{\perp} \ll 1$ the break occurs at k_d^{-1} and for $\beta_{\perp} \gg 1$, the break occurs at k_i^{-1} . The finding of (Chen et al. 2014) implies that the dissipation can undergo different processes, and as the solar wind MHD turbulence cascading proceeds, the process that has the largest of the characteristic scales prevails. In a more recent study, Woodham et al. (2018) using data from *Wind* spacecraft, performed an extensive study of the effect of β_p on the break frequency location. They concluded that the proton cyclotron resonance scale is most closely related to the spectral break when $\beta_p \sim 1$, but no definitive conclusions could be made at extreme β_p values. Wang et al. (2018) investigated the β_p dependence of the break frequency for a broad range of β_p from 0.005 to 20 and also found that cyclotron resonance best describes the spectral break location, although at extreme $\beta_p \ll 1$ and $\beta_p \gg 1$, inertial length scale or proton gyroradius can not be ruled out (Wang et al. 2018). In a recent work, Duan et al. (2020) used data from the *Parker Solar Probe* (*PSP*) to examine the radial evolution of ion spectral breaks during the second solar encounter, and obtained results that support Woodham et al. (2018); Wang et al. (2018).

While the above studies focus on the power spectra break of the quiet solar wind, another well-known and unique spectral feature, a spectral bump, has been first reported by Fairfield (1969). It has subsequently been observed upstream at multiple planetary bow shocks and has been referred to as the “1 Hz” wave in the literature (Brain et al. 2002; Le et al. 2013; Wilson 2016; Xiao et al. 2020). “1 Hz” waves are characterized, in the plasma rest frame, as small amplitude right-hand polarized

whistler waves generated upstream of collisionless shocks (i.e. planetary bow shocks) (Le et al. 2013; Wilson 2016). The bumps associated with these waves occur at frequencies (~ 1 Hz) higher than the spectral breaks, in the range of $20 - 100\Omega_{pi}$ (Hoppe et al. 1981). The detailed generation mechanism of these waves, however, is still unknown. Nevertheless, it has been noted by (Russell 2007) that the bump locations is proportional to magnetic field $|B|$. The *Mercury Surface, Space Environment, Geochemistry, and Ranging (MESSENGER)* spacecraft was launched in 2008. It has a few planetary flybys at both Venus and Mercury during which it traversed their bow shocks. During these flybys, MESSENGER was able to observe both the spectral break and the spectral bumps within a short period of time. As we show here, this provides a rare opportunity to examine the nature of the spectral break by using the spectral bump as a marker.

To better resolve spectral features, especially at frequencies close and higher than the spectral break, we adopt the wavelet transforms to examine the power spectral density (PSD). Wavelet analysis has become an increasingly popular tool to study a signals PSD due to the localization of the wavelet components in both frequency and time (Horbury et al. 2008; Podesta 2009; Woodham et al. 2018). Unlike the traditional Fourier transform, wavelet analysis produces smoother spectral plots, allowing spectral features to be better identified. For our analysis of both the spectral break and spectral bump associated with the “1 Hz” wave, wavelet analysis proves to be invaluable.

In this manuscript, we analyze the spectral break and spectral bump for 3 planet flybys, one at Venus, and two at Mercury using MESSENGER. We complement the MESSENGER periods by two periods from the Magnetospheric Multiscale (MMS) spacecraft at the Earth, covering a heliocentric distance from 0.34 to 1 au. The power spectral density is computed by wavelet analysis. Spectral breaks and spectral bumps at high frequency are identified. We compare the location of these two spectral features and find that the ratio of these two frequencies are largely independent of $|B|$ and r . We discuss the implication of our results on dissipation scale.

DATA AND METHODS

We use magnetic field data from the MESSENGER/MAG instrument (Anderson et al. 2007) for one flyby at Venus and two flybys at Mercury. For each flyby, two periods, one in the dawn side and one in the dusk side, are identified. During planetary flybys, *MESSENGER/MAG* recorded magnetic field data at 20 Hz, sufficient to observe ion scales. However, as noted by Anderson et al. (2007), there are possible digitization effects above 3 Hz, leading to some instrument noises. As we discuss below, however, except one spectral bump during a dusk period, the spectral breaks and bumps from MESSENGER/MAG observations occur below 3 Hz. We also use observations at 1 AU from the dual fluxgate magnetometers (Russell et al. 2016) onboard the Magnetospheric Multiscale (MMS) spacecraft. *MMS* provides magnetic field data at 16 Hz resolution (Russell 2007). Overall, since analysis is made from one spacecraft per period we negate any errors in the spacecraft measurements.

Figure 1 shows the trajectories of the three planetary flybys (6 periods) and the corresponding magnetic field measurements. Each period is four hours in duration. A one-hour sub-period, in each period, close to the bow shock, is colored in red for the dusk side and in orange for the dawn side (we adopt this color code convention throughout this work). The same one-hour period is shown as the shaded area on the right panels of Figure 1. Within this one-hour sub-period, the spacecraft is closer to the bow shock and the upstream “1 Hz” waves are observed (yielding a spectral bump). The remaining 3-hour sub-period is further away from the bow shock and no upstream “1 Hz” waves

are observed (yielding no spectral bump). Each period is also labeled with “I” or “II” to denote inbound or outbound trajectory.

The top panel is for June 5th, 2007, during the second Venus flyby. The middle and bottom panels are for January 14th and October 6th, 2008, during the first and second Mercury flybys, respectively. The bow shock positions shown in the left panels of Figures 1 and 2 are obtained using the functional form described in [Slavin et al. \(1984\)](#), and the dashed grey lines depict the average background magnetic field direction for our selected solar wind periods.

Similar to Figure 1, Figure 2 shows two *MMS* trajectories and magnetic field data for January 4th and 28th, 2020. The magnetic field data used was during the fast mode survey which has a resolution of 16 Hz. Unlike the trajectories of *MESSENGER* Venus/Mercury flybys, it is hard to denote “dawn” or “dusk” to these two *MMS* periods. However, the trajectory on the January 28th 2020 (hereafter TR1) is more along the Earth-Sun direction than that (hereafter TR2) of the January 4th 2020. Consequently we expect the 3-hour period from which we obtain the spectral break in TR1 is of more pristine solar wind than that in the corresponding 3-hour period in TR2. In the following we denote the trajectory on 2020 January 4 as “dusk side” and that on 2020 January 28 as “dawn side” in the following analysis.

To calculate the power spectral density (PSD), we follow [Podesta \(2009\)](#) using a wavelet analysis. Comparing to traditional spectral analysis methods based on Fourier transform, wavelet analysis yield smoother spectra, allowing clear identification of spectral features. Note that plasma data from *MESSENGER* is not available due to the sunshade restricting the Fast Imaging Plasma Spectrometer (FIPS) field of view ([Raines et al. 2011](#)). Previous investigations around Mercury have approximated solar wind conditions using the Ulysses spacecraft ([Korth et al. 2011](#)). [Baker et al. \(2011\)](#) estimated solar wind plasma properties at the three Mercury flybys using the WSA-Enlil model. Our result in this paper does not require knowledge of solar wind plasma property, although knowing solar wind speed helps to interpret our results. To obtain a rough estimate of the solar wind speed, we assume the solar wind can be approximated as quasi-steady structures and shift the *ACE* measurement to locations at the *MESSENGER* by co-rotation.

RESULTS AND DISCUSSION

We first calculate the power spectral density (PSD) for the eight periods we identify. Figure 3 shows the calculated wavelet spectrum for the 8 periods in Figure 1 and 2. The left panel shows the spectrum for the 3-hour period excluding the grey shaded areas in 1 and 2. The trace of the wavelet spectrum, shown as the black curve, is plotted in the spacecraft frame, and shifted down by a factor of 100. The top plot shows the trace in black and the corresponding fitting in orange. We fit the spectrum using a broken power-law ([Liu et al. 2020](#)), given by (1).

$$p(f) \propto \frac{f^\alpha}{(1 + (f/f_{brk})^\gamma)^\beta} \quad (1)$$

To perform the fitting we first find the inertial range spectrum using a least-squares procedure. We fit the inertial range for Mercury from 5.8×10^{-3} Hz to 0.44 Hz and Venus and Earth from 5.8×10^{-3} Hz to 0.17 Hz. We reduce the fitting range to ensure all fits are before the break location. Using the least-squares method, we set the value of α in equation (1). We next identify the best-fit parameters for the break location f_{brk} and spectral terms β and γ . We calculate the dissipation spectrum by

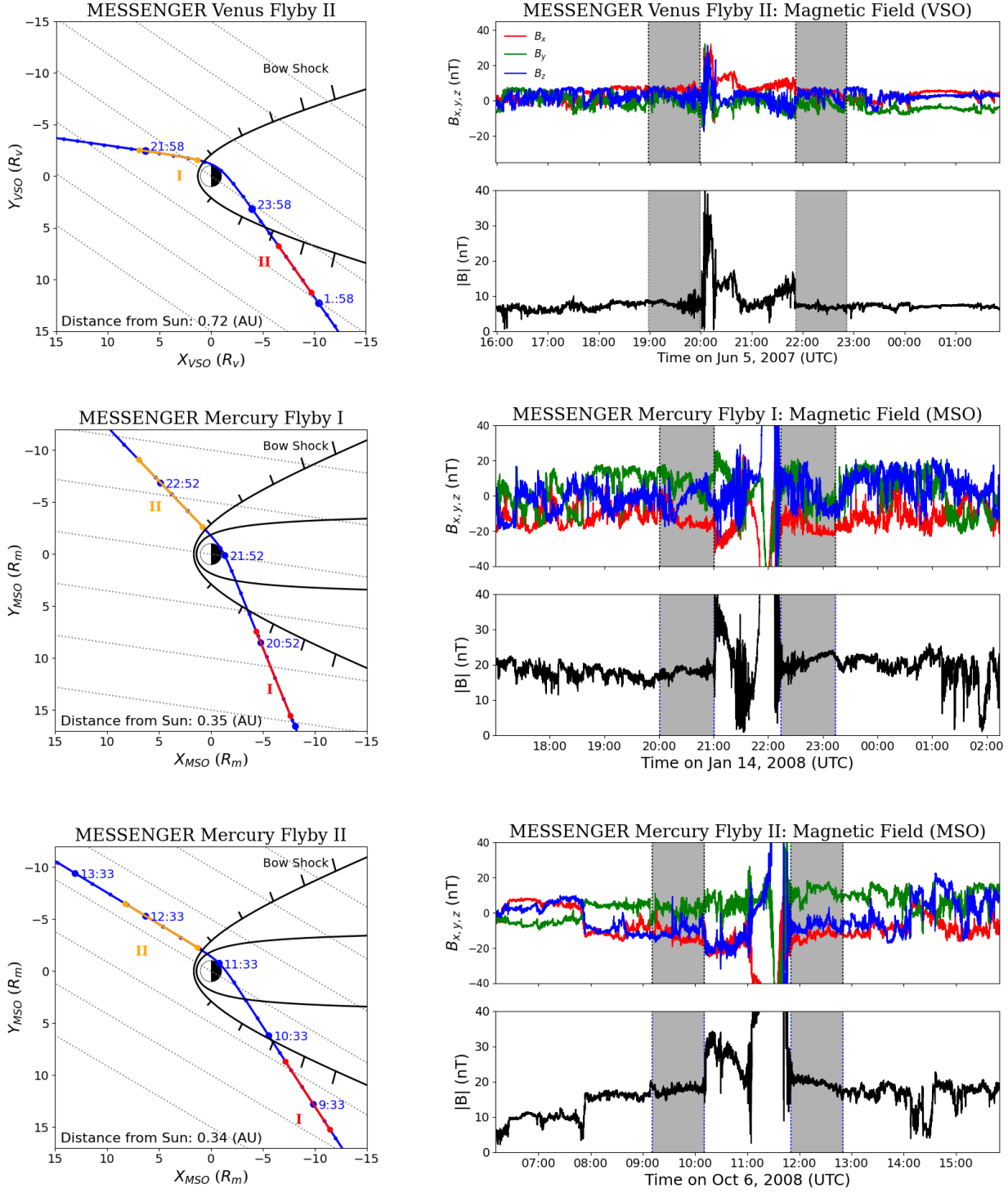


Figure 1. *MESSENGER* trajectories and magnetic fields during planetary flybys of Venus and Mercury. Left panels show the spacecraft trajectories during each planetary flyby. The red (orange) segments indicate periods of enhanced upstream wave activities in the dusk (dawn) side. The direction of spacecraft trajectory is shown in the order of I and II. Black curves show the bow shock, using approximation from Slavin et al. (1984). The right panels plot the corresponding magnetic field components and magnitude. Greyed periods correspond to the red and orange segments in the left panels.

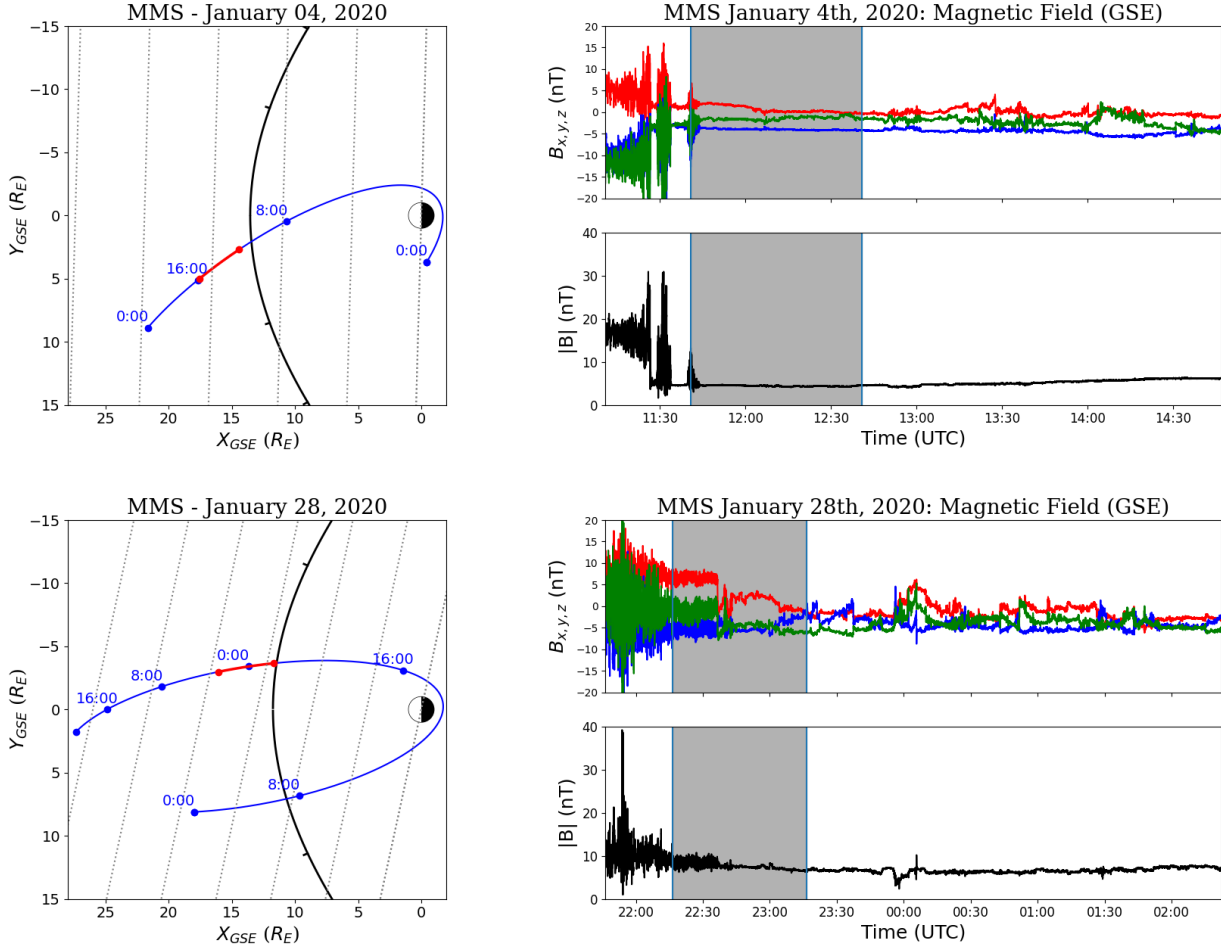


Figure 2. Similar to Figure 1 but for *MMS* observations. The left figures show *MMS* 1 spacecraft position during the two selected orbits. The regions marked in red correspond to the four hour duration post bow shock crossing. The panels to the right correspond to the magnetic field components and magnitudes. The greyed regions correspond the periods of enhanced wave activity. Note that the bow shock location for the January 28 event is shifted by 1.8 R_E from the model estimate since the magnetic field measurement for the period labeled by red is outside the bow shock.

taking $\alpha - \beta\gamma$. To determine the best fit, we used a χ^2 fitting routine, with the standard deviation being proportional to the PSD (Liu et al. 2020). To identify the bump location we calculated the local maxima in the frequency range from roughly 3 Hz to f_{brk} .

To guide the eyes, the blue dashed lines indicate the power law in the inertial range, and the dashed green lines indicate the power law in the dissipation range. The vertical solid green lines indicate the locations where the spectrum breaks occur. The right panel shows the spectrum for the full 4-hour period, including the grey shaded areas in Figure 1 and 2. The dashed green lines in the right panel correspond to the break locations identified from the left panels (the solid green lines). The vertical blue lines indicate the bump “peak” locations which are defined as the frequency f_i at which the 2-point slope of the log of power $P(f)$ drops the most, i.e., $(P^2(f_i)/(P(f_{i+1}) * P(f_{i-1}))$ is the maximum at the spectral bump frequency.

As expected, Figure 3 shows that the spectral bumps are due to wave activity occurring close to the bow shock, since they do not show up in the 3-hour period analysis and only show up in the 4-hour period. Furthermore, the spectral breaks are clearly seen for all the 3-hour data. For period “D”, corresponding to the “dusk” side of the Mercury flyby II, the fitting yield a dissipation spectral index of -2.48 , which is shallower than all other periods. A spectral break in this case is less clear than other periods.

One of our main findings is the correlation between the spectral break frequency f_{brk} and the location of the spectral bump f_{bump} . Since the former concerns the dissipation process at ion kinetic scale in the solar wind and the latter is related to whistler-mode waves that contains electron dynamics, the correlation between them is unexpected. Note that both the spectral break and the spectral bump occur in the same flyby, hence instrument uncertainties are mitigated.

Define η as $\eta = \ln(f_{bump}) - \ln(f_{brk})$, which is the log of the ratio f_{bump}/f_{brk} . The left panel of Figure 4 shows η as a function of radial distance, and the right panel shows η as a function of $|B|$. We distinguish the dawn and dusk observations using orange (dawn) and red (dusk) symbols. We see a clear separation of η between the dawn side trajectories and those in the dusk side. One possible explanation could be that the solar wind turbulence is affected by wave activity originated from the bow shock. Since the solar wind propagates from the dawn side to the dusk side, the dawn side sees a more pristine solar wind. Note that although the upstream waves are seen clearly as a bump for the 4-hour period and not shown in the 3-hour period, these waves can propagate obliquely to the upstream and interact with the solar wind turbulence at a lower frequency. This process will primarily affect the solar wind turbulence spectrum at the dusk side. As explained earlier, we categorize the MMS event on January 4th, 2020 as a dusk event, and that on January 28th, 2020 as a dawn event. As noted by Xiao et al. (2020), the distribution and characteristics of these upstream waves can differ in the quasi-parallel and quasi-perpendicular regions of the Bow Shock. This is perhaps not surprising as one expects that the relative configuration between the solar wind magnetic field and the bow shock may play a role in the generation of these upstream waves.

Table 1. The f_{bump} , $|B|$, and V_{sw}^* for the 8 periods in Figure 3.

Period:	A	B	C	D	E	F	G	H
f_{bump} (Hz):	1.337	1.337	2.421	2.673	2.673	3.597	1.634	1.707
$ B _{wave}$ (nT): ^a	7.61	7.32	19.10	18.77	20.86	17.94	8.416	5.314
$ B _{SW}$ (nT): ^b	7.02	6.98	19.73	17.83	17.07	13.40	6.65	5.53
V_{sw}^* (km/s): ^c	408.82	413.29	497.98	529.06	304.63	307.92	369.59	401.27

^a These are 5-minute magnetic field when the upstream waves are clearly seen, except the MMS events where we consider only the first 2.4-minutes.

^b These are average magnetic field for the 3-hour solar wind period.

^c For A to F, these are estimates of solar wind speeds using ACE data. G and H are direct MMS measurements. The value for period H is from a later period due to lack of data availability in period H.

Below we focus on the dawn side observations. We see that η is almost a constant as a function of r or $|B|$. Indeed, the range of η is from 1.21 to 1.41, translating to $f_{bump}/f_{brk} = 3.35$ to 4.1, a factor of 1.22. In comparison, the $|B|$ change from 7.4nT to 20.86nT, a factor of 2.6. This finding, that η , or f_{bump}/f_{brk} , is almost independent of r or $|B|$, is our most important result of this Letter. Note that

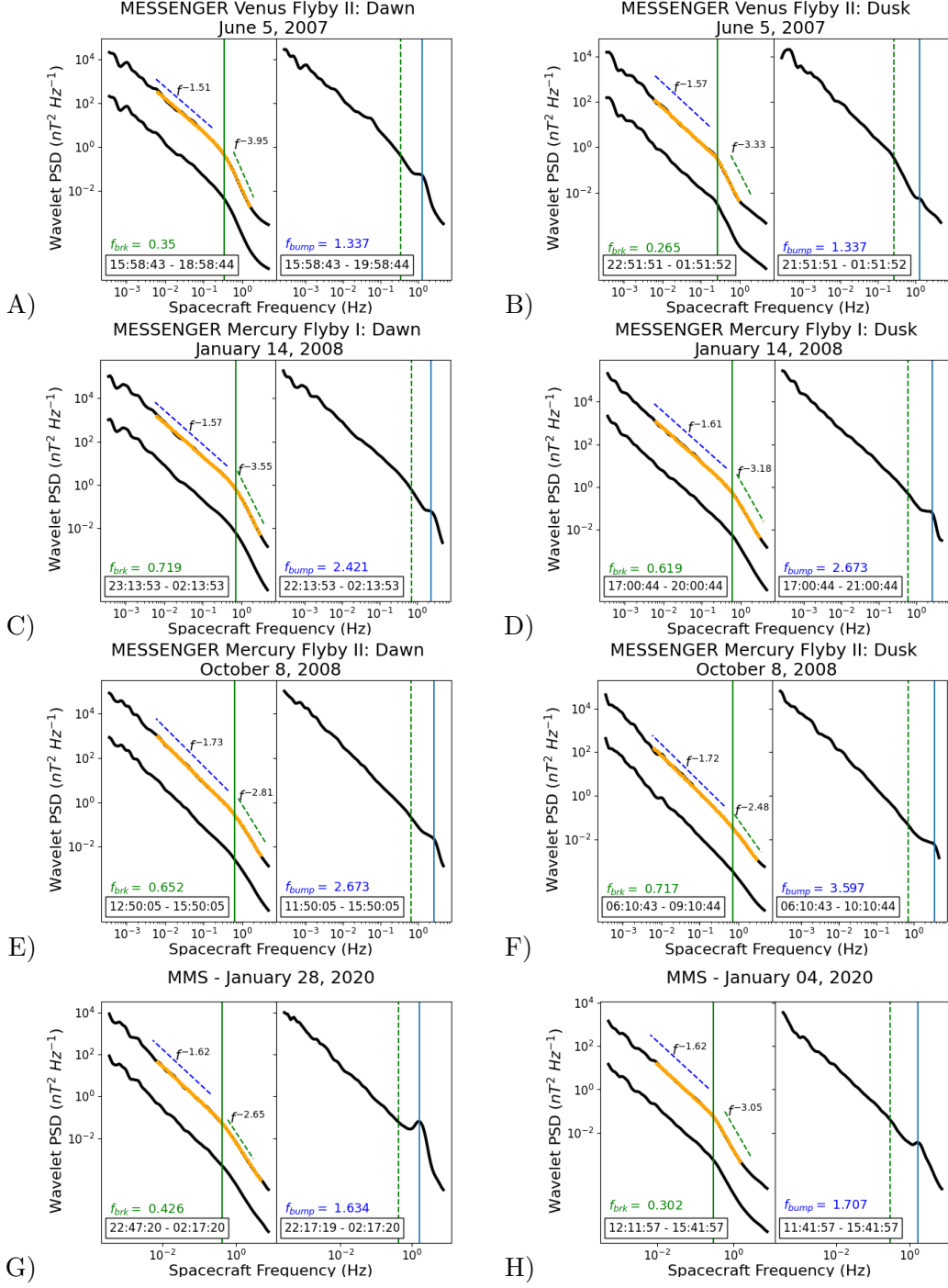


Figure 3. Power spectra for periods shown in Figure 1 and Figure 2. In each panel, the left side shows the 3-hour solar wind power spectra and the right side shows the full 4-hour solar wind power spectra. Significant upstream wave activities are only present close to the bow shock and result in a clear bump around 1 Hz for the 4-hour power spectra. The blue (green) dashed line is the fitting for the inertial (dissipation) range. The vertical solid green line indicates the frequency of the spectral break. The vertical blue solid line indicates the frequencies of the bump “peak”. The vertical dashed green line marks the same break frequency as the solid green line from the left side. The x-axis is the spacecraft frequency and the y-axis is the power density.

the variation of η may be even smaller. From the right panel of Figure 4, we see that the variation

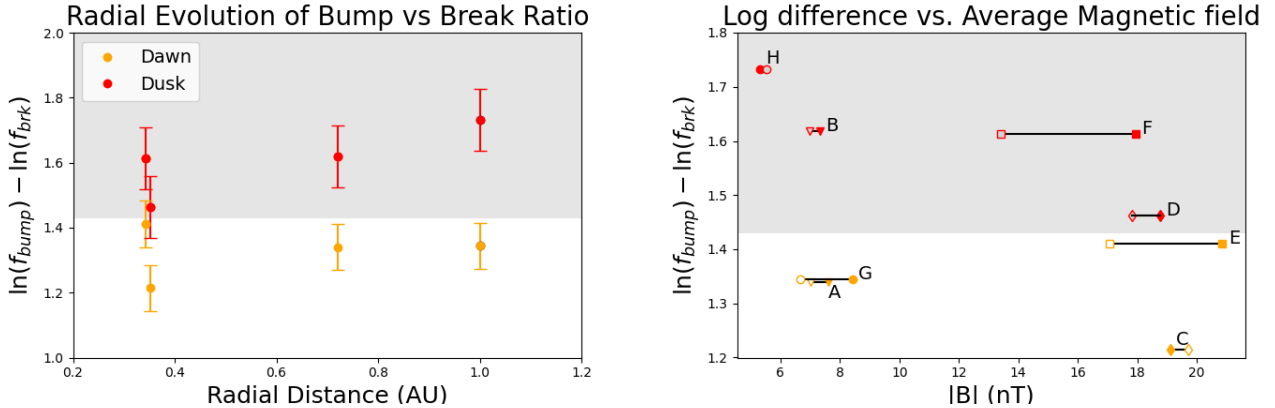


Figure 4. The quantity η as a function of r (left) and $|B|$ (right). The measurements are color coded with dawn events shown in orange and dusk events in red. Data shows a clear separation between dawn side events and dusk side events. The error bars represent the standard error by treating dawn side events and dusk side events separately. In the right panel, two B values are associated with each period. The solid symbol is a 5-minute average when the upstream wave activity is clearly seen and the outlined value is a 3-hour average in the solar wind. These $|B|$ values are listed in Table 1.

of η is largely due to period E, and from Table I, we see that the solar wind speed in period E is significantly smaller than other periods. Since f_{brk} is proportional to V_{sw} , this can lead to a larger η for period E. However, without plasma data from MESSENGER, the solar wind speed in Table I can only be regarded as a crude estimate.

We now discuss the implication of the very weak $|B|$ dependence of f_{bump}/f_{brk} on the mechanism of the spectral break. First we note that f_{bump} depends strongly on $|B|$. Earlier, Russell (2007) suggested that f_{bump} has a linear dependence on $|B|$. However, as shown in Table I, this dependence may be nonlinear, or if it is linear on $|B|$, then f_{bump} has to have an extra radial dependence. If we write,

$$f_{bump} = \text{const} \cdot \Omega_B^{\delta_1} \quad \text{or} \quad f_{bump} = \text{const} \cdot \Omega_B r^{\delta_2}, \quad (2)$$

then from Table I, one can estimate that $\delta_1 = 0.605$ and $\delta_2 = 0.402$. In both cases, f_{bump} has a clear B dependence. This, together with a B -independent η , imply that f_{brk} also has a clear $|B|$ dependence. Such a $|B|$ dependence argues strongly against k_i as the origin of the spectral break because $k_i = \Omega_p/V_A$ means that $f_{brk} = k_i * V_{sw}$ is $|B|$ independent. In comparison, the Larmor scale $k_L = \Omega_p/V_{th}$ is consistent with a $|B|$ -dependent (or $|B|$ -weakly-dependent) η . If we assume f_{bump} (and therefore f_{brk}) has a $|B|$ dependence as given by the second case in equation (2), then the Larmor scale provides a reasonable explanation for the spectral break if $V_{th} \sim r^{-\delta_2} \sim r^{-0.40}$. Recent PSP observations (Adhikari et al. 2020) suggest that the radial evolution of proton temperature can be approximated as $T \sim r^{-0.66}$, leading to a $V_{th} \sim r^{-0.33}$, slightly shallower than $r^{-0.40}$. The cyclotron resonance scale $k_d = \Omega_p/(V_A + V_{th}) = k_L/(1 + \beta_p^{-1/2})$ has a shallower dependence on r than the Larmor scale, and is also consistent with our observations. To discern these two, knowledge of plasma beta is crucial, which, however, is unavailable for MESSENGER observations. Regardless of the plasma beta in the three flybys, our result is consistent with that of Woodham et al. (2018); Duan et al. (2020) who argued that the dissipation occurs at cyclotron resonance scale when β_p is not extreme.

To summarize, in this paper we show that two frequencies: the one which is related to the “1-Hz” upstream waves at planetary bow shocks, f_{bump} , and the one which is related to the solar wind turbulence spectral break, f_{brk} , are strongly correlated. Their ratio, f_{bump}/f_{brk} , as measured from the dawn side flybys of MESSENGER, appears to be independent to $|B|$ and r . This observation, connecting two seemingly different phenomena, can be used to discern the underlying mechanisms of the spectral break. Alternatively, when a thorough understanding of the turbulence spectral break becomes available, our finding will allow us to better understand the underlying generation mechanisms of the upstream waves at planetary bow shocks.

ACKNOWLEDGMENTS

MT acknowledges the support of NASA FINESST Fellowship 80NSSC20K1516. This work is supported in part by NASA grants 80NSSC19K0075, and 80NSSC19K0831.

REFERENCES

Adhikari, L., Zank, G., Zhao, L., Nakanotani, M., & Tasnim, S. 2020, *Helios*, 2, 23

Alexandrova, O., Chen, C. H. K., Sorriso-Valvo, L., Horbury, T. S., & Bale, S. D. 2013, *Space Science Reviews*, 178, 101

Anderson, B. J., Acuña, M. H., Lohr, D. A., et al. 2007, in *The MESSENGER mission to Mercury* (Springer), 417–450

Baker, D. N., Odstrcil, D., Anderson, B. J., et al. 2011, *Planetary and Space Science*, 59, 2066

Bourouaine, S., Alexandrova, O., Marsch, E., & Maksimovic, M. 2012, *The Astrophysical Journal*, 749, 102

Bowen, T. A., Mallet, A., Bale, S. D., et al. 2020, *Physical Review Letters*, 125, 025102

Brain, D., Bagenal, F., Acuna, M., et al. 2002, *Journal of Geophysical Research: Space Physics*, 107, SMP

Bruno, R., & Carbone, V. 2013, *Living Reviews in Solar Physics*, 10, 2

Bruno, R., & Trenchi, L. 2014, *The Astrophysical Journal Letters*, 787, L24

Chen, C., Leung, L., Boldyrev, S., Maruca, B., & Bale, S. 2014, *Geophysical research letters*, 41, 8081

Duan, D., Bowen, T. A., Chen, C. H., et al. 2020, *The Astrophysical Journal Supplement Series*, 246, 55

Fairfield, D. H. 1969, *Journal of Geophysical Research*, 74, 3541

Hoppe, M., Russell, C., Frank, L., Eastman, T., & Greenstadt, E. 1981, *Journal of Geophysical Research: Space Physics*, 86, 4471

Horbury, T. S., Forman, M., & Oughton, S. 2008, *Physical Review Letters*, 101, 175005

Korth, H., Anderson, B. J., Zurbuchen, T. H., et al. 2011, *Planetary and Space Science*, 59, 2075

Le, G., Chi, P. J., Blanco-Cano, X., et al. 2013, *Journal of Geophysical Research: Space Physics*, 118, 2809

Leamon, R., Matthaeus, W. H., Smith, C. W., et al. 2000, *The Astrophysical Journal*, 537, 1054

Leamon, R. J., Matthaeus, W. H., Smith, C. W., & Wong, H. K. 1998, *The Astrophysical Journal Letters*, 507, L181

Leamon, R. J., Smith, C. W., Ness, N. F., Matthaeus, W. H., & Wong, H. K. 1998a, *Journal of Geophysical Research: Space Physics*, 103, 4775

Liu, Z., Wang, L., Wimmer-Schweingruber, R. F., Krucker, S., & Mason, G. M. 2020, *Journal of Geophysical Research: Space Physics*, 125, e2020JA028702

Perri, S., Carbone, V., & Veltri, P. 2010, *The Astrophysical Journal Letters*, 725, L52

Podesta, J. 2009, *The Astrophysical Journal*, 698, 986

Raines, J. M., Slavin, J. A., Zurbuchen, T. H., et al. 2011, *Planetary and Space Science*, 59, 2004

Russell, C. 2007, *Journal of atmospheric and solar-terrestrial physics*, 69, 1739

Russell, C., Anderson, B., Baumjohann, W., et al. 2016, *Space Science Reviews*, 199, 189

Schekochihin, A., Cowley, S., Dorland, W., et al. 2009, *The Astrophysical Journal Supplement Series*, 182, 310

Slavin, J., Holzer, R., Spreiter, J., & Stahara, S. 1984, *Journal of Geophysical Research: Space Physics*, 89, 2708

Smith, C. W., Hamilton, K., Vasquez, B. J., & Leamon, R. J. 2006, *The Astrophysical Journal Letters*, 645, L85

Telloni, D., Bruno, R., & Trenchi, L. 2015, *The Astrophysical Journal*, 805, 46

Verscharen, D., Klein, K. G., & Maruca, B. A. 2019, *Living reviews in solar physics*, 16, 1

Wang, X., Tu, C., He, J., & Wang, L. 2018, *The Astrophysical Journal*, 857, 136

Wilson, L. 2016, *Washington DC American Geophysical Union Geophysical Monograph Series*, 216, 269

Woodham, L. D., Wicks, R. T., Verscharen, D., & Owen, C. J. 2018, *The Astrophysical Journal*, 856, 49

Xiao, S., Wu, M., Wang, G., Chen, Y., & Zhang, T. 2020, *Planetary and Space Science*, 187, 104933